Microstructure and properties of LZQT600-3 HCCDIBs for plunger pump cylinder

*Chun-jie Xu[1, 2], Yuan-ying Jin[1, 2], Dong Ma[1, 2], Zhen Zhao[1, 2], Jia-wei Qi[1, 2], Shang Sui[1, 2], Xiang-quan Wu[1, 2], Can Guo[1, 2], Zhong-ming Zhang[1, 2], Yong-hui Liu[3], and Dan Shechtman[1, 2, 4]

1. School of Materials Science and Engineering, Xi'an University of Technology, Xi'an 710048, China

2. Xi'an Shechtman Nobel Prize New Materials Institute, Xi'an 710048, China

3. Tongchuan Huazhu Precision Technology Co., Ltd., Tongchuan 727100, Shaanxi, China

4. Faculty of Materials Science and Engineering, Technion-Israel Insititue of Technology, Haifa 3200003, Israel

Abstract: It is important to improve the comprehensive performance of the ductile iron bars (DIBs) for the cylinder block of the extra high pressure hydraulic plunger pump and accelerate the industrial application. In this work, the LZQT600-3 DIBs with the diameter of 145 mm were prepared by the horizontal continuous casting (HCC) process, that is, LZQT600-3 HCCDIBs. The microstructure and room temperature tensile properties of different sections [left-edge (surface layer), left-1/2R (left half of the radius), and the center of the HCCDIBs] were studied. The results show that the spheroidization of LZQT600-3 HCCDIBs matrix from the left-edge, left-1/2R to the center is at nodulizing grade II and above. As the cooling rate gradually decreases from surface to the center of the HCCIBs, the number of spheroidized graphite is gradually reduced, the size is gradually increased, the shape factor is decreased, and the pearlite content and lamellate spacing are increased. Along the horizontal direction of the section, the hardness of the material is distributed symmetrically around the center of the HCCDIBs. In the vertical direction, the hardness distribution in the center of the HCCDIBs is asymmetrical due to the gravity during the solidification process. Therefore, the microstructure in the lower part of the section solidifies relatively quickly. The left-edge has the best tensile mechanical properties, and the ultimate tensile strength, yield tensile strength and elongation are 597.3 MPa, 418.5 MPa and 9.6%, respectively. The tensile fracture belongs to the ductile-brittle hybrid fracture. The comprehensive performances of LZQT600-3 HCCDIBs meet the actual application requirements of ultra-high pressure hydraulic plunger pump cylinder.

Keywords: horizontal continuous casting (HCC); nodular cast iron; ductile iron bars; microstructure; mechanical properties

CLC numbers: TG143.5   **Document code:** A   **Article ID:** 1672-6421(2024)02-197-08

1 Introduction

In recent years, with the development of the hydraulic industry towards high speed, high precision and high efficiency, higher requirements have been put forward for hydraulic pumps [1-3]. During the operation of the plunger pump, the cylinder block is subjected to huge torsional torque and tensile stress when rotating at high speeds

*Chun-jie Xu

Male, born in 1971, Ph. D, Professor. He has been working in the field of preparation of metallic materials and their composites. In particular, his research focuses on developing new preparation technics of metallic materials to expand their applications. His academic research has led to the publication of more than 180 papers.

E-mail: xuchunjie@xaut.edu.cn

for oil absorption and draining. Due to defects such as sand holes, inclusions, and porosity, traditional sand cast ductile iron has insufficient pressure and leakage resistance, no longer meeting the material requirements of high-performance hydraulic pumps such as plunger pumps [4-6]. Horizontal continuous casting iron bars (HCCIBs) have a uniform and compact structure, free from casting defects such as slags and sand inclusions in sand casting, have the characteristics of dense microstructure, fine grain size, large numbers of graphite spheres, high rate of spheroidization and spheroidization level, excellent comprehensive mechanical properties and good machining performance, especially excellent pressure resistance, and have been widely utilized in machinery, hydraulic and other industries or fields [7, 8]. Therefore, in recent years, some enterprises have used LZQT500-7 horizontal continuous casting ductile

iron bars (HCCDIBs) to produce plunger pump cylinders [6, 7]. However, the plunger pump cylinder block will still be stuck during operation. The friction occurred in a relatively short period of time leads to the failure and the shortening of service life. These problems are caused by the nonuniform cross-section microstructure and uneven mechanical properties of large-diameter HCCIBs [8], and their nonuniform section sensitivity. At the same time, as the technical requirements for the plunger pump continue to evolve, there is also a simultaneous gradual improvement on the performance requirements of the HCCIBs. Copper atoms have high solid solubility in austenite, which can form a layer of copper-rich barrier layer on the surface of graphite sphere in the eutectic stage and increase the diffusion resistance of carbon atoms. Thus, it can hinder the diffusion of carbon atoms into the graphite spheres and further inhibit growth of the graphite spheres, increasing the number of pearlite [8]. Therefore, the addition of copper elements can promote graphitization of ductile iron, significantly increase and refine the pearlite. This reduces the unevenness of the microstructure of the piston pump and improves the mechanical properties. In this study, by adding a certain amount of copper to LZQT500-7, LZQT600-3 can be obtained, which maybe further improve the hardness and tensile strength of the plunger pump. It is a pearlitic matrix ductile iron with better strength and hardness than other common grades of cast iron bars, so the practical application with the hope to use the LZQT600-3 to replace LZQT500-7 [7].

In this work, the microstructure and mechanical properties of different positions of the large-diameter LZQT600-3 HCCDIBs were discussed, aiming to provide basic data for the research on reducing the section sensitivity of the microstructure and properties of HCCDIBs, so as to expand the application of HCCDIBs in the field of the extra high pressure hydraulic plunger pump.

2 Experimental procedure

The LZQT600-3 HCCDIBs with 145 mm in diameter were prepared in a ZSL-08 HCC production line and produced by Shaanxi Hua'an Cast Iron Profile Co. The duplex melting process was carried out in a 5 t medium-frequency induction furnace, and the tapping temperature was from 1,480 °C to 1,520 °C. The spheroidization and inoculation were achieved by feeding wire, using 2.3 m spheroidized cored wire (designations YDB3030, with 30%–35% Mg, 2%–3% RE, 40%–46% Si, 2%–3% Ca, <1.0% Al, <1.5% MgO, Bal. Fe) and 2.3 m inoculant cored wire (designations YDB005, with 68%–70% Si, 4%–6% Ba, 1%–3% Ca, 1%–2% Al, Bal. Fe) per 100 kg molten iron. Before spheroidization and inoculation, according to the weight ratio with molten iron, 0.7% SiC with size of 0.5–5 mm, 0.4% 75SiFe with size of 10–30 mm, and 0.5% Cu electrolytic copper plate were added to the bottom of a 1,000 kg molten iron dam-type ladle, which were melted and inoculated during pouring with molten iron. The melted iron was transferred into the holding furnace at temperatures from

1,360 to 1,420 °C. The final measured chemical composition of HCCDIBs is 3.02% C, 2.42% Si, 0.32% Mn, 0.35% Cu, 0.04% P and 0.01% S, and the carbon equivalent (CE) is 3.90%. The Machinery Industry Standard of China (MISC) (JB/T 10854-2019, Horizontal continuous cast iron bars) provides designation is LZQT600-3, the size of sample is shown in Fig. 1.

The horizontal direction of sample was symmetric, the sampling locations were taken from ~20 mm away from the left-edge, left half of the radius (left-1/2R) and the center of cross-section, respectively, to analyze the microstructure by SEM, hardness and tensile properties of HCCDIBs at different positions, as shown in Fig. 1. Among them, four tensile samples were taken from each position, and the mean value was taken as the final result. The dimension of dog-bone shape tensile specimens is shown in Fig. 2.

Three groups of different graphite sphere number data were obtained in the same sampling part, according to the national standard GB/T 9441-2009 "Ductile Iron Metallurgical Inspection". The number of graphite spheres n in the area of the field of view $A_1 (\text{mm}^2)$ is:

$$n = n_1 + \frac{n_2}{2} \qquad (1)$$

where n_1 is the number of graphite spheres falling entirely within the field of view (pcs), n_2 is the number of graphite spheres cut by the boundary of the field of view (pcs).

The number of graphite spheres per unit area n_F is:

$$n_F = \frac{n}{A_1} \qquad (2)$$

where n is the number of graphite spheres (pcs) within the area A_1.

The metallographic corrosion solution was a 3.5% nitrate alcohol solution. Specimens for microstructure analysis were characterized by an Olympus-GX53 optical microscope, the fracture morphology was investigated by a SM-6700F scanning electron microscope (SEM). Image J analysis
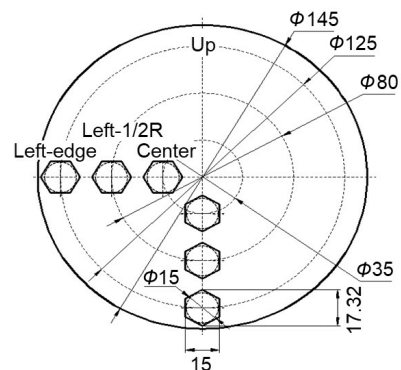

Fig. 1: Samples position for microstructural observation and tensile test
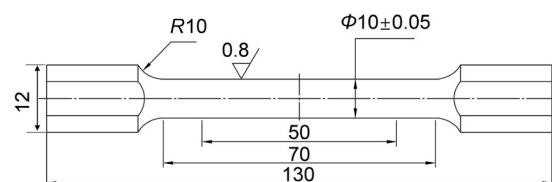

Fig. 2: Schematic diagram of tensile sample (unit: mm)

software was used to count the number and measure the diameter of graphite spheres in different parts of the ductile iron in the polished state, and a shape factor F is as follows [9]:

$$F = \frac{4\pi S}{L} \tag{3}$$

where S and L are the area of graphite sphere (μm^2) and the circumference of the nodules (μm), respectively. A value of $F=1$ corresponds to a perfectly round particle, and the shape becomes more irregular with decreasing F.

The number of pearlites in different parts was also quantitatively described by Image J software. Since the metallographic images obtained under light microscopy graphite spheres and pearlites in the corroded state of ductile iron have similar gray levels, it is inconvenient to count the number of single pearlites. The statistical scheme of this experiment is that the nodules and pearlite as a whole statistical to count the number of pearlites in different sampling parts, while the pearlite content η_P can be calculated as:

$$\eta_P = \frac{A_P}{A_2} \times 100\% \tag{4}$$

where A_P is pearlite area (mm^2); A_2 is total field of view (mm^2).

Three images were taken from each sample for statistics, and the results were averaged.

Due to the randomness orientation of the pearlite eutectic mass, the pearlite lamellar spacing observed after erosion is usually not the true lamellar spacing d_0 of the pearlite. Because there is an angle θ between the observed surface of the sample and the real pearlite lamellar normal, the observed lamellar spacing d is greater than the real lamellar spacing d_0, as shown in Fig. 3.

Obviously,

$$d_0 = d \cdot \cos\theta \tag{5}$$

Related literatures [10, 11] give the following relation through derivation and analysis:

$$\overline{d_0} = \frac{2}{\pi}\overline{d} \tag{6}$$

where $\overline{d_0}$ is a mean value of true pearlite lamellar spacing d_0 (nm), $\overline{d}$ is mean pearlite apparent lamellar spacing d (nm).

The pearlite apparent lamellar spacing was measured by circumferential measurement method. Ten different fields of view were randomly selected for each sample, and five circles were measured under each field of view, and the results were averaged. The circumferential diameter was 5 μm. The calculation equation [13] is as follows:

$$d = \frac{L_c}{2N_c} \tag{7}$$

where d is pearlite apparent lamellar spacing (nm) measured by circumferential measurement, L_c is circumference (nm), N_c is the number of points at which the circumference intersects the pearlite lamellar.

The hardness test was conducted on an HB-3000 Brinell hardness tester. The diameter D of the steel ball was 5 mm,

the load P was 7,500 N, and the load holding time was 10 s, the test points were horizontal and vertical direction of the profile section passing through the center, and three points were tested every 10 mm and the average was used as the fnal value. Tensile testing was carried out on the WDW-200 microcomputer control electronic universal testing machine with a strain rate of 8.33×10^{-4} s^{-1} at room temperature.
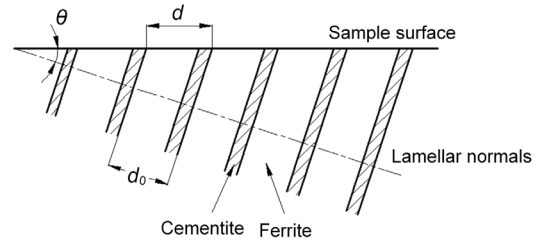

Fig. 3: Relationship between actual and apparent layers of pearlite

3 Results and discussion

3.1 Microstructure characterization

Figure 4 shows the graphite and matrix structures morphology of LZQT600-3 HCCDIBs with 145 mm in diameter at different positions. It can be found from Fig. 4 that the diameter of the graphite sphere from the left edge to the center gradually increases, and the spheroidization grade becomes worse. According to the American Society for Testing and Materials (ASTM) A247 international standard, after the spheroidization of graphite, the iron matrix incorporates the nodules of nodulizing grade I, size 8 close to the surface; nodulizing grade I-II, size 7 at the left-1/2R from the surface; and nodulizing grade II, size 7 in the center of the HCCDIBs. It can be seen that the grain size from the surface to the center gradually increases, and the pearlite quantity increases. Quantitative statistics of Image J show that the pearlite quantities in the left-edge, left-1/2R and center are 23.7%, 34.2% and 45.5%, respectively.

Diameter distribution and shape factor statistical results of graphite nodules in different locations are shown in Fig. 5 and Fig. 6. The number of graphite nodules in the left-edge, left-1/2R and center of HCCDIBs is 356, 269 and 235 pieces·mm^{-2}, respectively, which shows a decreasing trend. The average diameters of graphite spheres are 19.62, 22.65 and 24.24 μm, respectively, the diameter of graphite nodules in the center is the largest (24.24 μm). The average shape factors of the graphite spheroids in the surface, left-1/2R and center are 0.810, 0.789 and 0.750, respectively. With the decrease of the cooling rate and the extension of the solidification time, the sphericity of the graphite spheroids deteriorates.

The SEM images of pearlite of LZQT600-3 HCCDIBs at different positions are shown in Fig. 7. The lamellae structure of ferrite and cementite is clearly visible, and the lamellae spacing of pearlite increases from the surface to the center. Quantitative analysis shows that the lamellar spacing of left-edge, left-1/2R and center is 118.6 nm, 127.3 nm and 135.5 nm, respectively.

The difference of the lamellar spacing between the left-edge and the center of LZQT600-3 HCCDIBs is caused by the different cooling rates and solidification times of molten iron at different positions in the HCC process [7]. According to Luan et al. [14], the fitting relation of grain size λ and solidification cooling rate V is $\lambda=85.1V^{-0.35}$. The cooling rate V of left-edge, left-1/2R and center can be calculated as 89.96, 43.90 and 36.16 °C·s^{-1},

respectively. From the edge to the center, the molten iron on the surface of the HCCDIBs is directly in contact with the graphite in the water-cooled iron sleeve graphite crystallizer, and the molten iron in the left-1/2R and the center is generally solidified outside the crystallizer through the heat conduction of the solidified surface structure. At the edge of the sample, the faster cooling rate results in a high rate of nucleation,
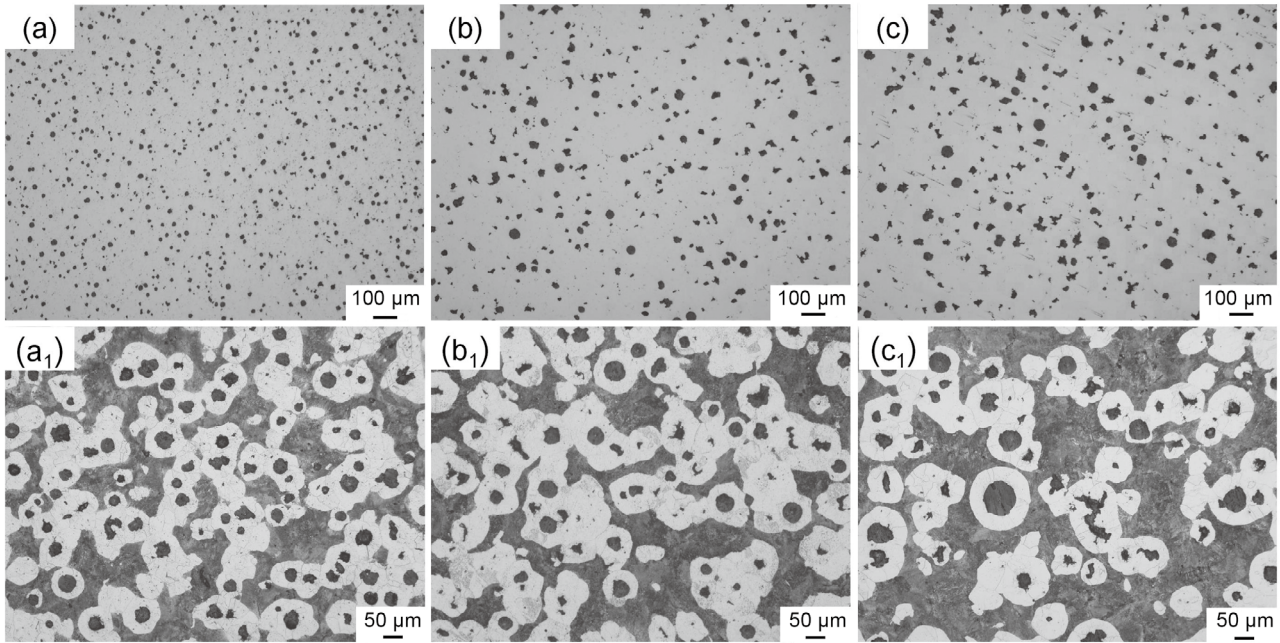

Fig. 4: Graphite (a, b, c) and matrix (a_1, b_1, c_1) morphology of LZQT600-3 HCCDIBs at different positions: (a) and (a_1) left-edge; (b) and (b_1) left-1/2R; (c) and (c_1) center
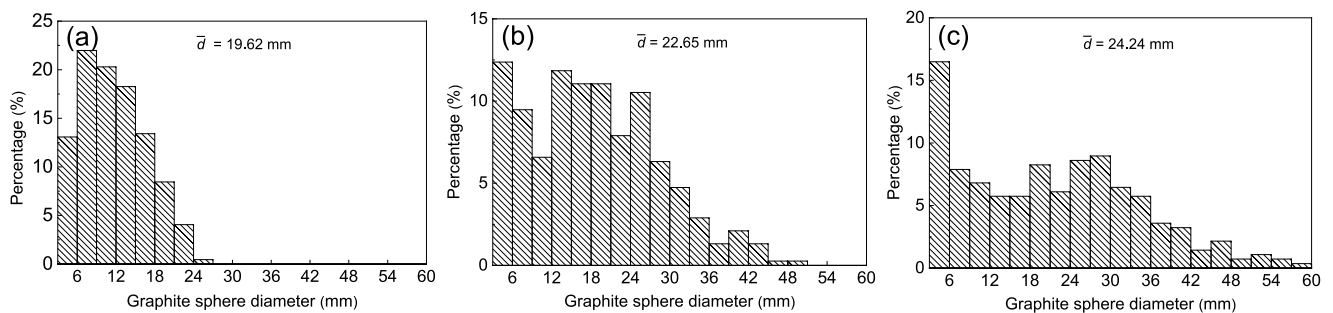

Fig. 5: Diameter distribution of graphite nodules of LZQT600-3 HCCDIBs at different positions: (a) left-edge; (b) left-1/2R; (c) center
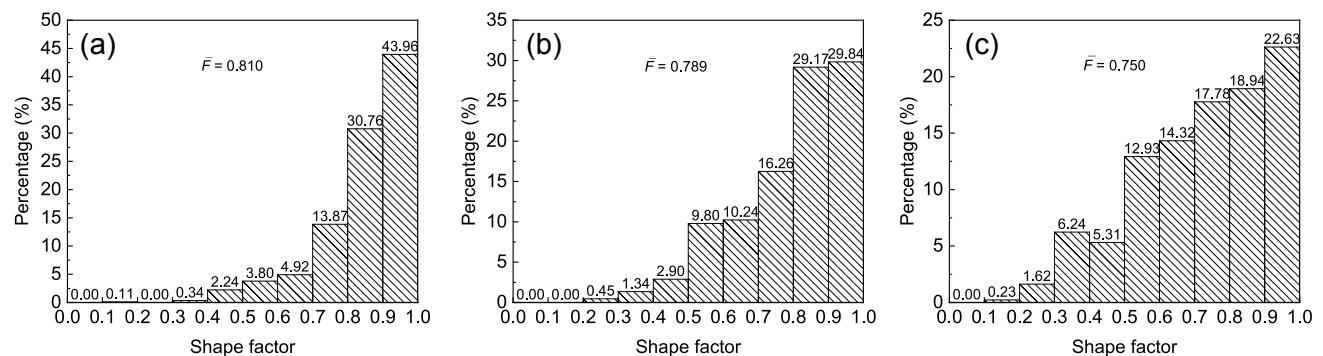

Fig. 6: Shape factor of graphite nodules of LZQT600-3 HCCDIBs at different positions: (a) left-edge; (b) left-1/2R; (c) center
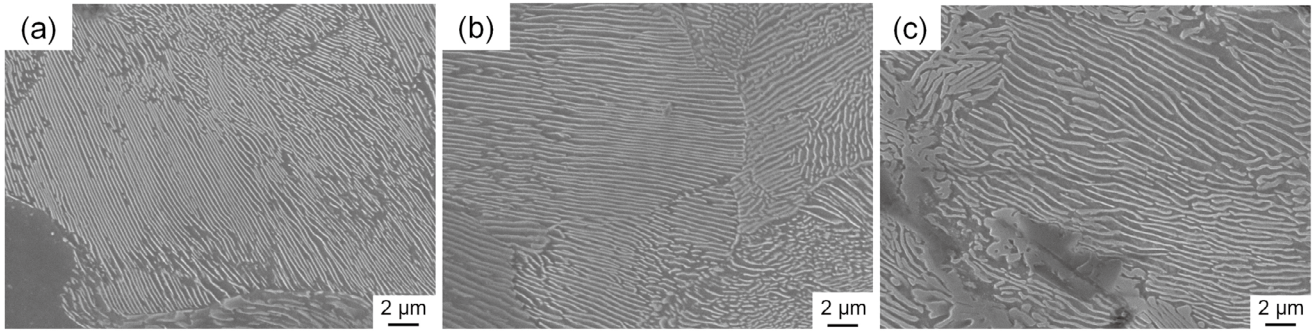
Fig. 7: SEM images of pearlite of LZQT600-3 HCCDIBs at different positions: (a) left-edge; (b) left-1/2R; (c) center

therefore the number of graphite spheres in this area is larger, the sphere diameter is small, the microstructure is fine; and cooling rate at the left-1/2R and the center of the iron is slow, the nucleation rate is greatly reduced, the iron stays for a long time, such a solidification environment provides conditions for further growth of the graphite spheres and grains, so the number of graphite spheres in this part is small, the sphere diameter is large, and the microstructure is coarse. Thus, it can be concluded that, a higher cooling rate leads to a higher nucleation rate, resulting in a larger number of graphite nodules in a smaller size. At the same time, it should also be noted that in order to improve efficiency and stable production, in the actual production of HCCDIBs, after pulling out the crystallizer, the outside surface of the HCCDIBs should be sprayed with spray mist for secondary cooling, which accelerates the cooling of the solidified surface microstructure and reduces the eutectoid transition time. It can be seen that the high cooling rate leads to a short residence time in the eutectoid transition stage, which is not conducive to the diffusion of atoms such as C, resulting in insufficient austenite transformation, and ultimately fewer pearlite in the surface matrix, and smaller spacing between the pearlite lamellae. On the contrary, the amount of pearlite increases and the spacing between the lamellar increases.

3.2 Mechanical properties

The Brinell hardness of LZQT600-3 HCCDIBs at different positions is shown in Fig. 8. It can be seen that the hardness distribution along the horizontal direction of the cross section is basically symmetric around the center of the HCCDIBs,

decreasing from the edge to the center which is related to the microstructure. The hardness at the top and bottom section of the cross section is slightly different, and the hardness at the bottom section is 3 HBW higher than that of the top section, which is caused by gravity. The microstructure at the lower part of the section solidifies relatively quickly, namely, the so-called liquid center is tilted upward, and the upper and lower parts are asymmetrical [12]. As the result, the microstructure in bottom section is finer which causes a higher hardness.

The tensile test results from different positions of LZQT600-3 HCCDIBs are shown in Fig. 9. It can be seen that the tensile strengths at the left-edge, left-1/2R and the center are 597.3, 576.3 and 547.9 MPa, and the elongations are 9.6%, 8.7% and 4.7%, respectively; the left-edge has the best strong plastic matching. Combined with the quantitative analysis of the graphite quantity, shape factor, diameter distribution, pearlite quantity and lamellar spacing of the graphite spheres, it can be seen that the number of graphite spheres from the left edge to the center decreases, the diameter of the spheres increases, and the spheroidization deteriorates. The mechanical properties of nodular cast iron are determined by the combination of structural characteristics, especially the morphology of graphite [13, 15-19]. In the process of tensile, when the graphite sphere is separated from the matrix, the holes formed by the graphite sphere with better spheroidization are more round and more difficult to cause stress concentration [16]. Therefore, it can withstand larger loads in the process of tensile, and has higher strength and better elongation.
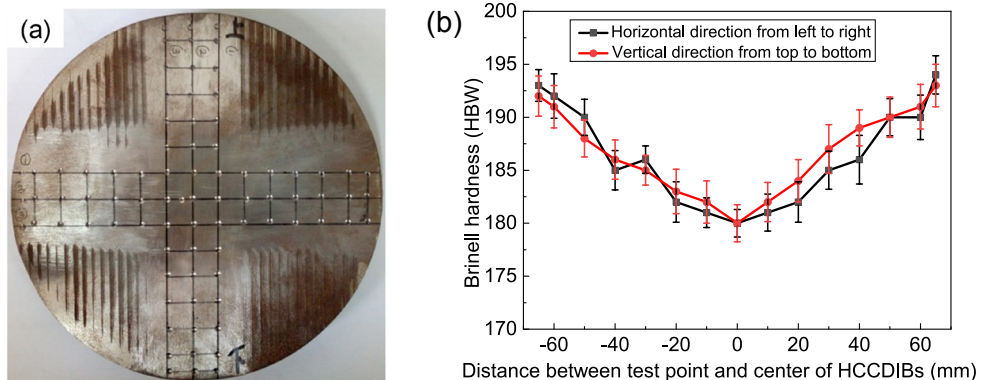

Fig. 8: Brinell hardness of LZQT600-3 HCCDIBs at different positions: (a) Brinell hardness test position;
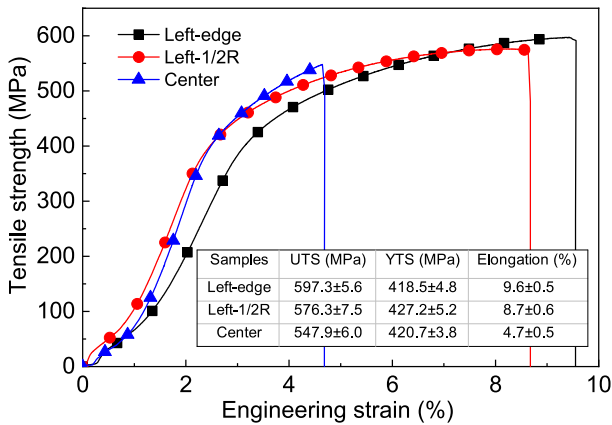**(b) hardness distribution**

Fig. 9: Tensile properties curves of HCCDIBs with diameter of 145 mm

The embedded table in Fig. 9:

Samples	UTS (MPa)	YTS (MPa)	Elongation (%)
Left-edge	597.3±5.6	418.5±4.8	9.6±0.5
Left-1/2R	576.3±7.5	427.2±5.2	8.7±0.6
Center	547.9±6.0	420.7±3.8	4.7±0.5

The macro morphology of the tensile fracture of LZQT600-3 HCCDIBs at different positions is shown in Figs. 10(a), (b) and (c). It can be seen that the fracture of the three samples is relatively flat, especially the left-edge fracture. The surface of the left-1/2R and the center fracture is relatively rough. In particular, the fracture surface morphology of the center sample is obviously different from that of other fractures which divides the two regions [Fig. 10(c)]. Figures 10(c_{11})–(c_{13}) and Figs. 10(c_{21})–(c_{23}) respectively correspond to the enlarged morphologies of the two regions C_1 and C_2 in the center. Due to the small pearlite content in C_2 region compared with C_1 region, a large area of "river" pattern and obvious cleavage fracture characteristics can be seen in the C_2 region. While the ductile fracture characteristics are obvious in the C_1 region with lots of dimples.

It can be seen that the fracture mainly reflects three main characteristics: Firstly, dimples are distributed over the surface of each fracture, as shown in Figs. 10(a_1), (b_1) and (c_{11}). Further magnification shows that these dimples are centered on graphite spheres, as shown in Figs. 10(a_2), (b_2), and (c_{12}). The size of the dimples is closely related with the size of the graphite spheres, the larger the graphite spheres, the larger the dimples. The dimples are caused by the uneven deformation of graphite spheres and matrix. In the process of plastic deformation of the matrix, the deformation capacity of the graphite spheres is lower than that of the matrix, so a large stress concentration will be generated in the interface of the graphite spheres/matrix. On the one hand, the graphite spheres are broken during tensile testing, and the broken graphite spheres can be observed at the center of the dimple, as shown in Figs. 10(a_2), (b_2) and (c_{12}). The way of crack propagation of HCCDIBs is along the boundary between graphite nodules and matrix when the tensile normal fracture occurs. On the other hand, due to the induced cracks at the interface of the graphite sphere/matrix, the graphite sphere is degloved and the dimples without the graphite sphere can be seen. Secondly, secondary dimples, which are one order of magnitude smaller than primary dimples, can be observed in the boundary of primary dimples (dimples with graphite spheres as the core), corresponding to Regions A, B and C_1 in Fig. 10(a_2), Fig. 10(b_2)

and Fig. 10(c_{12}). Thirdly, a small amount of "river" pattern formed by dissociation "step" can be observed on the fracture surface in Figs. 10(c_{13}) and (c_{23}), which is a typical cleavage plane, and the main fracture characteristics are transgranular fractures. At the same time, obvious lamellar pearlite fracture exists on the fracture surface, as shown in Figs. 10(a_3), (b_3) and (c_{13}).

By comparing the fracture morphology of the samples at the three different positions, it can be seen that the fracture surface has the characteristics of the ductile-brittle hybrid fracture, and the fracture mechanism is microvoid coalescence fracture and quasi-cleavage fracture. This is due to the different graphite sphere numbers, sizes, roundness and the different contents of pearlite in the matrix microstructure of different samples.

Compared with LZQT500-7, after adding a small amount of Cu, the developed LZQT600-3 improves the microstructure and comprehensive mechanical properties of DIBs. At the same time, it meets the basic requirements of chemical composition, microstructure and performance of materials in the current plunger pump drawings. The plunger pump cylinder prepared by LZQT600-3 has been applied to industrial production.

4 Conclusions

(1) The LZQT600-3 HCCDIBs with a diameter of 145 mm incorporates the nodules of nodulizing grade I, size 8 close to the left-edge; nodulizing grade I-II, size 7 at the left-1/2R; and nodulizing grade II size 7 in the center of the HCCDIBs.

(2) The graphite nodules density at about 20 mm away from the bar left-edge, left-1/2R and in the center are 356, 269, and 235 pieces·mm^{-2}, average diameters are 19.62, 22.65, and 24.24 μm, and the shape factors are 0.810, 0.789 and 0.750, and the cooling rates are 89.96, 43.90, and 36.16 °C·s^{-1}, respectively. The content of pearlite in the matrix is 23.7%, 34.2% and 45.5%, and the lamellar spacing of pearlite is 118.6, 127.3 and 135.5 nm, respectively.

(3) The horizontal section hardness is basically symmetrical about the center of the LZQT600-3 HCCDIBs with 145 mm in diameter. In the vertical direction, the hardness is slightly different up and down due to the action of gravity, and the hardness of the lower side is higher than that of the upper side. The tensile mechanical properties of the left-edge and left-1/2R of HCCDIBs are better than that of the center. The tensile strength of the left-edge, left-1/2R and center is 597.3, 576.3 and 547.9 MPa, and the elongation is 9.6%, 8.7% and 4.7%, respectively. The LZQT600-3 HCCDIBs used for plunger pump cylinder have reached the practical application level.

(4) Dimples exist at different sampling parts of the tensile fracture surface that increase in size as the graphite spheres size gets larger. The fracture surface has the characteristics of the ductile-brittle hybrid fracture and the fracture mechanism is microvoid coalescence fracture and quasi-cleavage fracture. The crack propagation way of HCCDIBs is along the boundary between graphite nodules and substrate when the tensile normal fracture occurs.
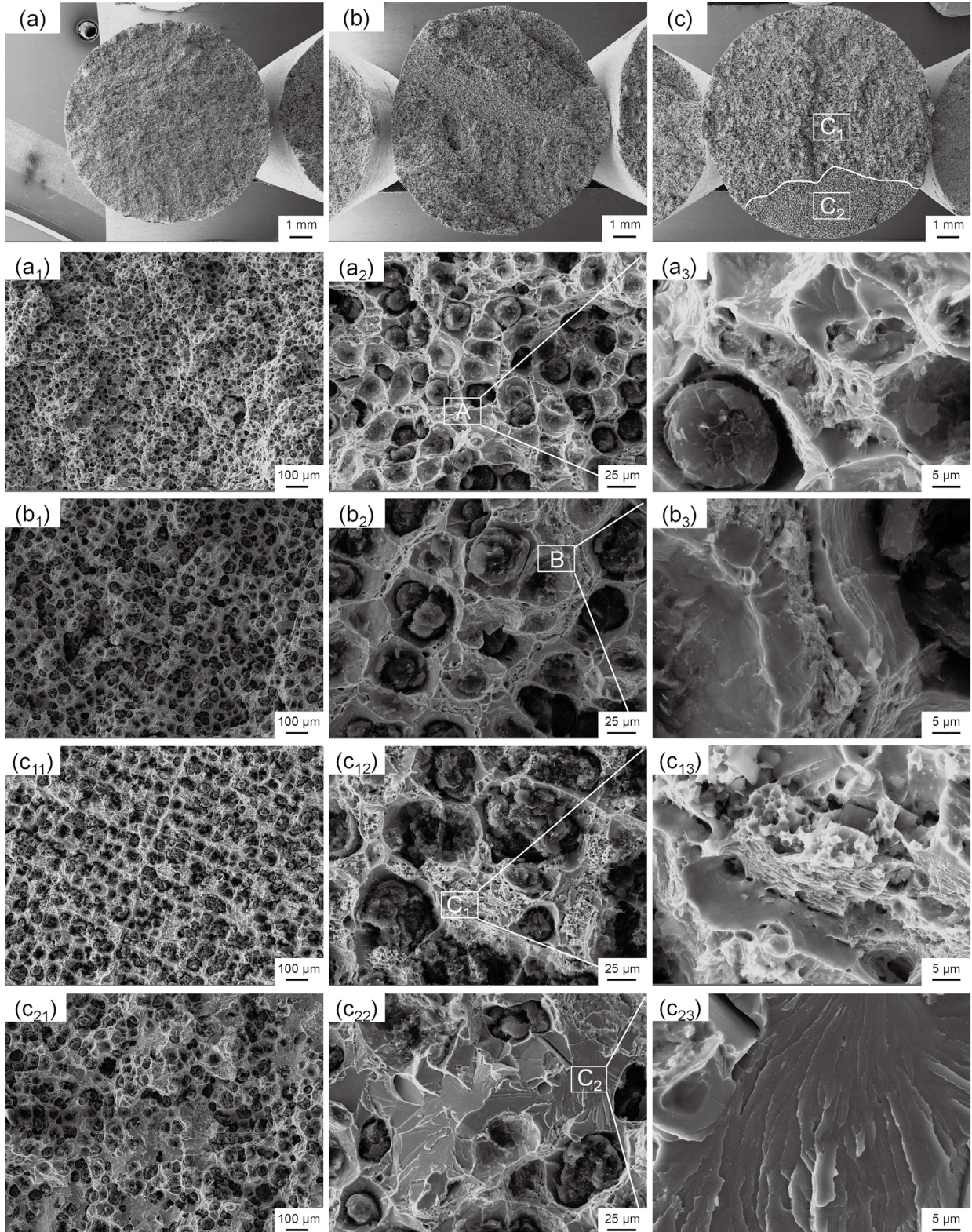
Fig. 10: SEM images of tensile fracture of LZQT600-3 HCCDIBs at different positions: (a, a₁, a₂, a₃) left-edge; (b, b₁, b₂, b₃) left-1/2R; (c, c₁₁, c₁₂, c₁₃, c₂₁, c₂₂, c₂₃) center

Acknowledgments

Conflict of interest

The authors declare that they have no known competing financial interests or personal relationships that could have appeared to influence the work reported in this paper.

References

[1] Lian Z H, Liu Y, Lin T J, et al. Study on the fluid flow rule of five-cylinder plunger pump hydraulic end. Petroleum, 2017, 4(4): 457–465.

[2] Chao Q, Xu Z, Tao J F, et al. Capped piston: A promising design to reduce compressibility effects, pressure ripple and cavitation for high-speed and high-pressure axial piston pumps. Alexandria Engineering Journal, 2023, 62: 509–521.

[3] Zhou Y, Huang Z Q, Bu Y, et al. Simulation studies on drilling mud pump plunger seal failure under ultrahigh pressure and ultradeep conditions. Engineering Failure Analysis, 2014, 45: 142–150.

[4] Nilsson K F, Vokál V. Analysis of ductile cast iron tensile tests to relate ductility variation to casting defects and material microstructure. Materials Science and Engineering: A, 2009, 502(1–2): 54–63.

[5] Xu C J, Dai P, Zhang Z Y, et al. Effect of austempering parameters on microstructure and mechanical properties of HCC ductile iron dense bars. China Foundry, 2015, 12(2): 104–110.

[6] Xu C J, Zhao Z, Lei Y, et al. Microstructure and properties of ductile iron bars for plunger pump prepared by horizontal continuous casting process. China Foundry, 2019, 16(2): 118–125.

[7] Xu C J, Xu X F, Zhao Z, et al. Horizontal continuous casting technology of cast iron and application of dense bars. Foundry Technology, 2017, 38(11): 2559–2564. (In Chinese)

[8] Wang Z H, Mei W, Cai Y W, et al. Effect of shrinkage porosity on mechanical properties and fracture characteristics of ferritic ductile iron EN-GJS-400-18-LT. Foundry, 2021, 70(8): 47–55. (In Chinese)

[9] Hsu C H, Lin K T. A study on microstructure and toughness of copper alloyed and austempered ductile irons. Materials Science and Engineering: A, 2011, 528(18): 5706–5712.

[10] Benedetti M, Fontanari V, Lusuardi D. Effect of graphite morphology on the fatigue and fracture resistance of ferritic ductile cast iron. Engineering Fracture Mechanics, 2019, 206: 427–441.

[11] Yan H, Wang A H, Xiong Z T, et al. Microstructure and wear resistance of composite layers on a ductile iron with multicarbide by laser surface alloying. Applied Surface Science, 2010, 256: 7001–7009.

[12] Peng C, Liu R Y. Secant method for measuring pearlite lamellar spacing in steel. Physical Test, 1990, 8(5): 40–44. (In Chinese)

[13] Jiang B Y, Meng L G, Ya B, et al. Study on the horizontal continuous casting of Cu-based bulk metallic glass slab. Journal of Non-Crystalline Solids, 2020, 543: 120150.

[14] Zhou Y T, Shao X H, Zheng S J, et al. Structure evolution of the Fe_3C/Fe interface mediated by cementite decomposition in cold-deformed pearlitic steel wires. Journal of Materials Science & Technology, 2022, 101: 28–36.

[15] Luan B F, Zhang D, Guo N, et al. Quantitative characterization on microstructure of hot rolled hypereutectoid steel wire rod for bridge cable. Transactions of Materials and Heat Treatment, 2011, 32(7): 78–82. (In Chinese)

[16] Du B N, Hu Z Y, Sheng L Y, et al. Tensile, creep behavior and microstructure evolution of an as-cast Ni-based K417G polycrystalline superalloy. Journal of Materials Science & Technology, 2018, 34: 1805–1816.

[17] Liu Y Z, Li Y F, Xing J D, et al. Effect of graphite morphology on the tensile strength and thermal conductivity of cast iron. Materials Characterization, 2018, 144: 155–165.

[18] Isabel H, Mohamed B B, Anthony T, et al. Graphite nodule morphology as an indicator of the local complex strain state in ductile cast iron. Materials and Design, 2013, 52: 524–532.

[19] Francesco I, Vittorio D C. Influence of the graphite elements morphology on the fatigue crack propagation mechanisms in a ferritic ductile cast iron. Engineering Fracture Mechanics, 2016, 167: 248–258.

[20] Diao X G, Ning Z L, Cao F Y, et al. Graphite morphology evolution during melt holding of ductile iron. Key Engineering Materials, 2010, 457: 31–36.